

# Pseudo Test-Retest Evaluation of Millimeter-Resolution Whole-Brain Dynamic Contrast-enhanced MRI in Patients with High-Grade Glioma


Yannick Bliesener, MS • R. Marc Lebel, PhD • Jay Acharya, MD • Richard Frayne, PhD • Krishna S. Nayak, PhD

From the Ming Hsieh Department of Electrical and Computer Engineering, Viterbi School of Engineering, University of Southern California, 3740 McClintock Ave, EEB 400, Los Angeles, CA 90089-2564 (Y.B., K.S.N.); GE Healthcare, Calgary, Canada (R.M.L.); Department of Radiology, University of Calgary, Calgary, Canada (R.M.L.); Seaman Family MR Research Centre, Foothills Hospital, Calgary, Canada (R.M.L., R.F.); Department of Radiology, Keck School of Medicine, University of Southern California, Los Angeles, Calif (J.A., K.S.N.); and Departments of Radiology and Clinical Neuroscience, Hotchkiss Brain Institute, University of Calgary, Calgary, Canada (R.F.). Received September 4, 2020; revision requested October 21; final revision received January 14, 2021; accepted February 16. Address correspondence to Y.B. (e-mail: [bliesene@usc.edu](mailto:bliesene@usc.edu)).

Supported by the National Institutes of Health (grant R33-CA225400) and the Canadian Cancer Society (grant 704210).

Conflicts of interest are listed at the end of this article.

See also the editorial by Lenkinski in this issue.

Radiology 2021; 300:410–420 • <https://doi.org/10.1148/radiol.2021203628> • Content codes: 

**Background:** Advances in sub-Nyquist-sampled dynamic contrast-enhanced (DCE) MRI enable monitoring of brain tumors with millimeter resolution and whole-brain coverage. Such undersampled quantitative methods need careful characterization regarding achievable test-retest reproducibility.

**Purpose:** To demonstrate a fully automated high-resolution whole-brain DCE MRI pipeline with 30-fold sparse undersampling and estimate its reproducibility on the basis of reference regions of stable tissue types during multiple posttreatment time points by using longitudinal clinical images of high-grade glioma.

**Materials and Methods:** Two methods for sub-Nyquist-sampled DCE MRI were extended with automatic estimation of vascular input functions. Continuously acquired three-dimensional k-space data with ramped-up flip angles were partitioned to yield high-resolution, whole-brain tracer kinetic parameter maps with matched precontrast-agent T1 and  $M_0$  maps. Reproducibility was estimated in a retrospective study in participants with high-grade glioma, who underwent three consecutive standard-of-care examinations between December 2016 and April 2019. Coefficients of variation and reproducibility coefficients were reported for histogram statistics of the tracer kinetic parameters plasma volume fraction and volume transfer constant ( $K^{\text{trans}}$ ) on five healthy tissue types.

**Results:** The images from 13 participants (mean age  $\pm$  standard deviation, 61 years  $\pm$  10; nine women) with high-grade glioma were evaluated. In healthy tissues, the protocol achieved a coefficient of variation less than 57% for median  $K^{\text{trans}}$ , if  $K^{\text{trans}}$  was estimated consecutively. The maximum reproducibility coefficient for median  $K^{\text{trans}}$  was estimated to be at 0.06  $\text{min}^{-1}$  for large or low-enhancing tissues and to be as high as 0.48  $\text{min}^{-1}$  in smaller or strongly enhancing tissues.

**Conclusion:** A fully automated, sparsely sampled DCE MRI reconstruction with patient-specific vascular input function offered high spatial and temporal resolution and whole-brain coverage; in healthy tissues, the protocol estimated median volume transfer constant with maximum reproducibility coefficient of 0.06  $\text{min}^{-1}$  in large, low-enhancing tissue regions and maximum reproducibility coefficient of less than 0.48  $\text{min}^{-1}$  in smaller or more strongly enhancing tissue regions.

Published under a CC BY 4.0 license.

Online supplemental material is available for this article.

Dynamic contrast-enhanced (DCE) MRI enables assessment of neurovascular parameters by monitoring enhancement patterns in tissue after injection of contrast agent. Such parameters could provide markers for tumor grading in patients with high-grade glioma (1,2) and for early brain tumor response to antiangiogenic therapy (3). Brain lesions commonly exhibit large regions of spatial heterogeneity or thinly enhancing rims around necrotic cores; in addition, multifocal metastases may be visible throughout the entire brain (4). Effective markers therefore require high-spatiotemporal-resolution whole-brain DCE MRI protocols, as well as accurate and reproducible tracer kinetic parameters (3,5,6).

Many attempts have been made to achieve desired spatial resolution and coverage while preserving rapid sampling

of the temporal evolution of contrast agent dynamics. Although direct estimation of tracer-kinetic parameters from undersampled MRI raw data exists (7,8), more commonly, constrained reconstruction algorithms reconstruct the image time series in an intermediate step (9–11) or simultaneously to tracer-kinetic estimation (12). This can be advantageous because it offers great flexibility in the estimation of nuisance parameters, such as the vascular input function (VIF), which is commonly done on the basis of image data.

Extensive efforts by the Radiological Society of North America Quantitative Imaging Biomarkers Alliance DCE MRI task force and other groups have resulted in standardization and characterization of Nyquist-sampled DCE MRI (13). Although much research has been devoted to obtaining 20- to 50-fold undersampled parallel imaging

## Abbreviations

COV = coefficient of variation, DCE = dynamic contrast enhanced,  $K^{\text{trans}}$  = volume transfer constant, MOCCO = model consistency constrained, RC = reproducibility coefficient, ROI = region of interest, SPSENSE = sparse sensitivity encoded, VIF = vascular input function,  $v_p$  = plasma volume fraction

## Summary

Evaluation of longitudinal millimeter-resolution whole-brain dynamic contrast-enhanced MRI bounds the coefficient of variation for median volume transfer constant to be less than 57% in healthy tissue regions.

## Key Results

- In this prospective study of 13 participants, an automated, sparsely sampled dynamic contrast-enhanced (DCE) MRI reconstruction offered spatial resolution of  $0.9 \text{ mm} \times 1 \text{ mm} \times 2 \text{ mm}$  at 5-second temporal resolution and full brain coverage.
- In healthy tissues, pseudo test-retest in sparsely sampled DCE MRI estimated median of volume transfer constant ( $K^{\text{trans}}$ ) with maximum reproducibility coefficient (RC) of  $0.06 \text{ min}^{-1}$  in large, low-enhancing tissue regions and maximum RC of less than  $0.48 \text{ min}^{-1}$  in smaller or more strongly enhancing tissue regions.
- Millimeter-resolution whole-brain DCE MRI achieved maximum coefficient of variation in healthy tissues of less than 57% for median  $K^{\text{trans}}$ .

techniques (9–12), a similar characterization has not yet been performed for high-spatiotemporal-resolution whole-brain DCE MRI systems with sparse sampling.

Characterization of measurement uncertainty relies on reproducibility studies in controlled test-retest settings. These tend to be time consuming, resource demanding, and ethically challenging to justify. Recruitment of patients with high-grade glioma is further complicated by disease severity, which lowers willingness of outpatients to accept the inconvenience of non-standard-of-care retest DCE MRI examinations. This unwillingness prevents the full development and characterization of candidate markers for individualized therapy and clinical trials (3,14,15). To determine the intrinsic method uncertainty and hence sample size required for larger clinical trials (15), the use of clinical posttreatment data could be an alternative to obtaining true test-retest data. By setting the focus on stable tissue types with varying parameter magnitudes, worst-case estimates for parameter uncertainty in the target brain tumor tissue could be inferred.

In this work, we demonstrate a fully automated, high-spatiotemporal-resolution, whole-brain DCE MRI pipeline with 30-fold sparse undersampling and no user interaction required. We estimate the reproducibility of this proposed pipeline on the basis of reference regions of stable tissue types during multiple posttreatment time points in patients with brain tumors.

## Materials and Methods

### Participants

In a retrospective study, we estimated reproducibility of the proposed pipeline among participants with high-grade glioma who underwent three consecutive standard-of-care examinations (mean interval between examinations, 64 days; range, 35–231 days). All data were acquired with a single clinical 3.0-T MRI machine (MR750, GE Healthcare) with a 12-channel head-neck-spine

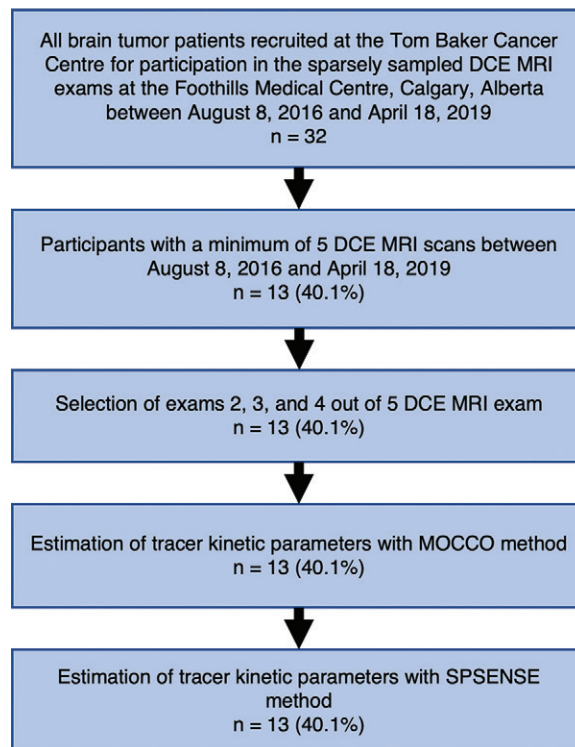


**Figure 1:** Flowchart of participants and exclusion criteria. Between August 2016 and April 2019, a total of 32 patients with brain tumors were recruited for sparsely sampled dynamic contrast-enhanced (DCE) MRI protocol. After exclusion of all participants with fewer than five DCE MRI examinations in this time period, data from second, third, and fourth DCE MRI examinations were used for reconstruction with model consistency constrained (MOCCO) and sparse sensitivity encoding (SPSENSE) methods.

receiver coil between August 2016 and April 2019 at the Seaman Family MR Research Centre, Foothills Medical Centre (Calgary, Alberta, Canada). Participants were recruited from the Tom Baker Cancer Centre and provided written informed consent. Data were acquired under a protocol approved by the relevant local institutional review board.

Participants were selected from an ongoing imaging study of high-grade gliomas. The current study included the first 13 participants with a minimum of five longitudinal MRI examinations among a total cohort of 32 participants; the second through fourth examinations were used in the current study. Participants with fewer than five MRI examinations were excluded. Figure 1 shows a flowchart of participant recruitment and exclusion criteria. Participants received heterogeneous and often-changing pharmacologic therapy during the three time points. Medications included dexamethasone, temozolomide, and clobazam.

### Sparse DCE MRI Data Acquisition

Three-dimensional k-space data were continuously acquired during a time window of 9.6 minutes (field of view,  $240 \times 240 \times 240 \text{ mm}^3$ ; voxel size,  $0.94 \times 1.0 \times 2.0 \text{ mm}^3$ ; echo time msec/repetition time msec, 1.9/5). During this time window, the contrast agent (Gadovist, Bayer AG) at a dose of  $0.1 \text{ mL/kg}$  body weight was intravenously injected. The readout dimension was fully sampled while the phase encode dimensions were acquired along rasterized spiral-in trajectories. The  $B_1^+$  maps were estimated by

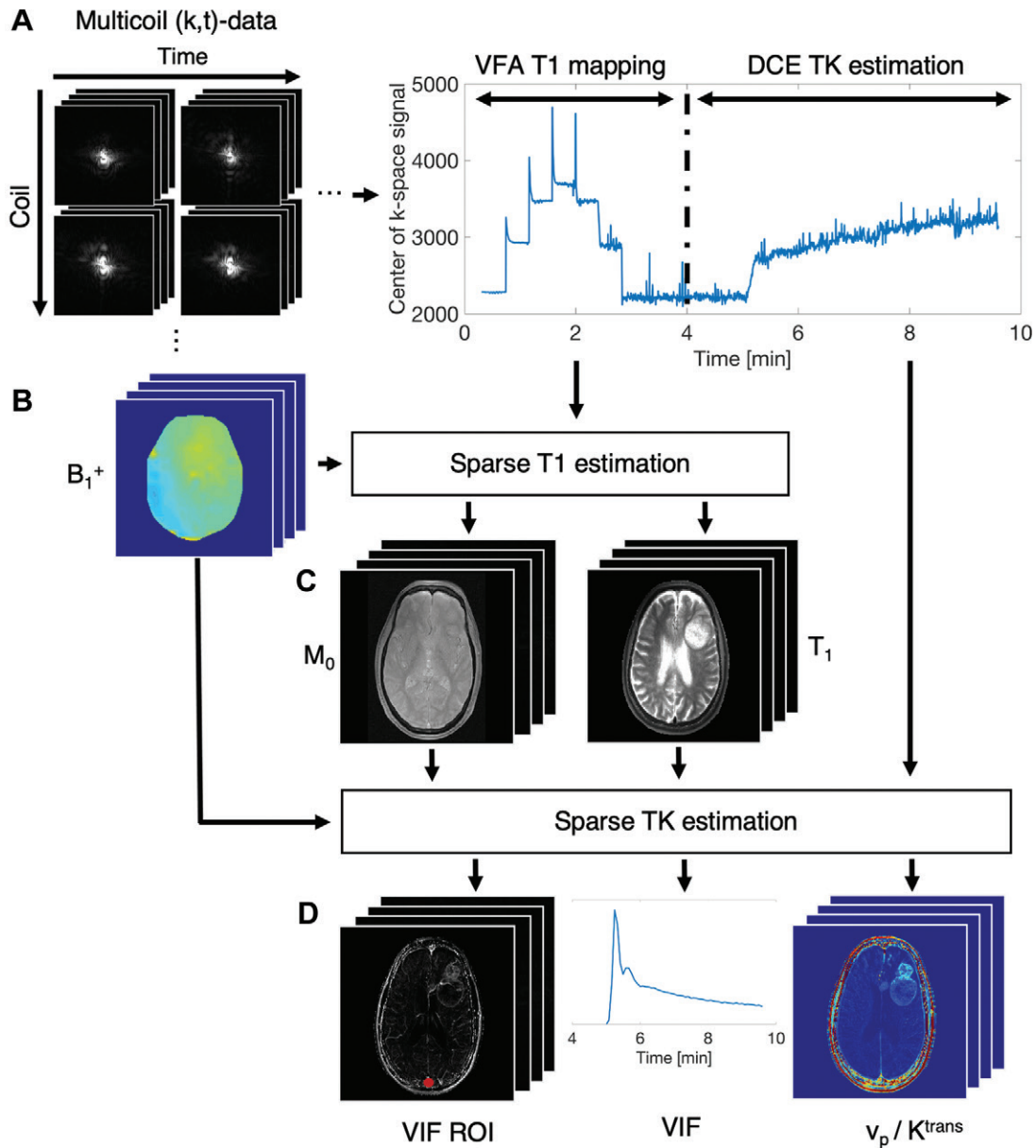


**Figure 2:** Image shows schematic of pipeline. A, Three-dimensional k-space data are continuously acquired over time window of approximately 10 minutes (cubic 240-mm<sup>3</sup> field of view with voxel size of 0.94 × 1.0 × 2.0 mm<sup>3</sup>, echo time of 1.9 msec, and repetition time of 5 msec). During first part of examination, flip angle is successively ramped up from 1.5° to 15° in seven logarithmically spaced steps to yield variable-flip-angle (VFA) measurements for high-resolution whole-brain T1 mapping. VFA data are used with B, calibration B<sub>1</sub><sup>+</sup> map to generate, C, T1 and M<sub>0</sub> maps before administration of contrast material. D, Vascular input function (VIF) regions of interest (ROIs), VIF, and tracer kinetic (TK) parameter maps for plasma volume fraction ( $v_p$ ) and volume transfer constant ( $K^{trans}$ ) are estimated from second part of k-space data (in A), which monitors contrast enhancement at 5-second temporal resolution. DCE = dynamic contrast enhanced.

the vendor-provided Bloch-Siegert method (16). During the first 170 seconds of the MRI examination, the flip angle was successively ramped up from 1.5° to 15° in seven logarithmically spaced steps to yield variable flip-angle measurements for high-spatio-temporal-resolution whole-brain T1 mapping (17). The variable flip-angle data were used with a calibration B<sub>1</sub><sup>+</sup> map to generate precontrast-agent T1 and M<sub>0</sub> maps. The last part of the k-space data after bolus arrival was binned to 5-second temporal resolution to monitor contrast enhancement and allow for estimation of vascular input functions and tracer kinetic parameter maps. Figure 2 illustrates data acquisition and reconstruction steps.

### Sparse DCE-MRI Reconstruction Methods

Lebel et al (10) demonstrated reconstruction of high-spatial-resolution whole-brain DCE MRI time series from highly undersampled raw k-space data for tracer-kinetic parameter estimation. Guo et al (12) demonstrated joint estimation of tracer-kinetic parameter maps and patient-specific VIF. In the current study, we extended the sparse SENSE (SPSENSE) framework by Lebel et al (10) and the model consistency constrained (MOCCO) method by Guo et al (12) with an automated delineation of brain vessels based on common image/time series features in the literature

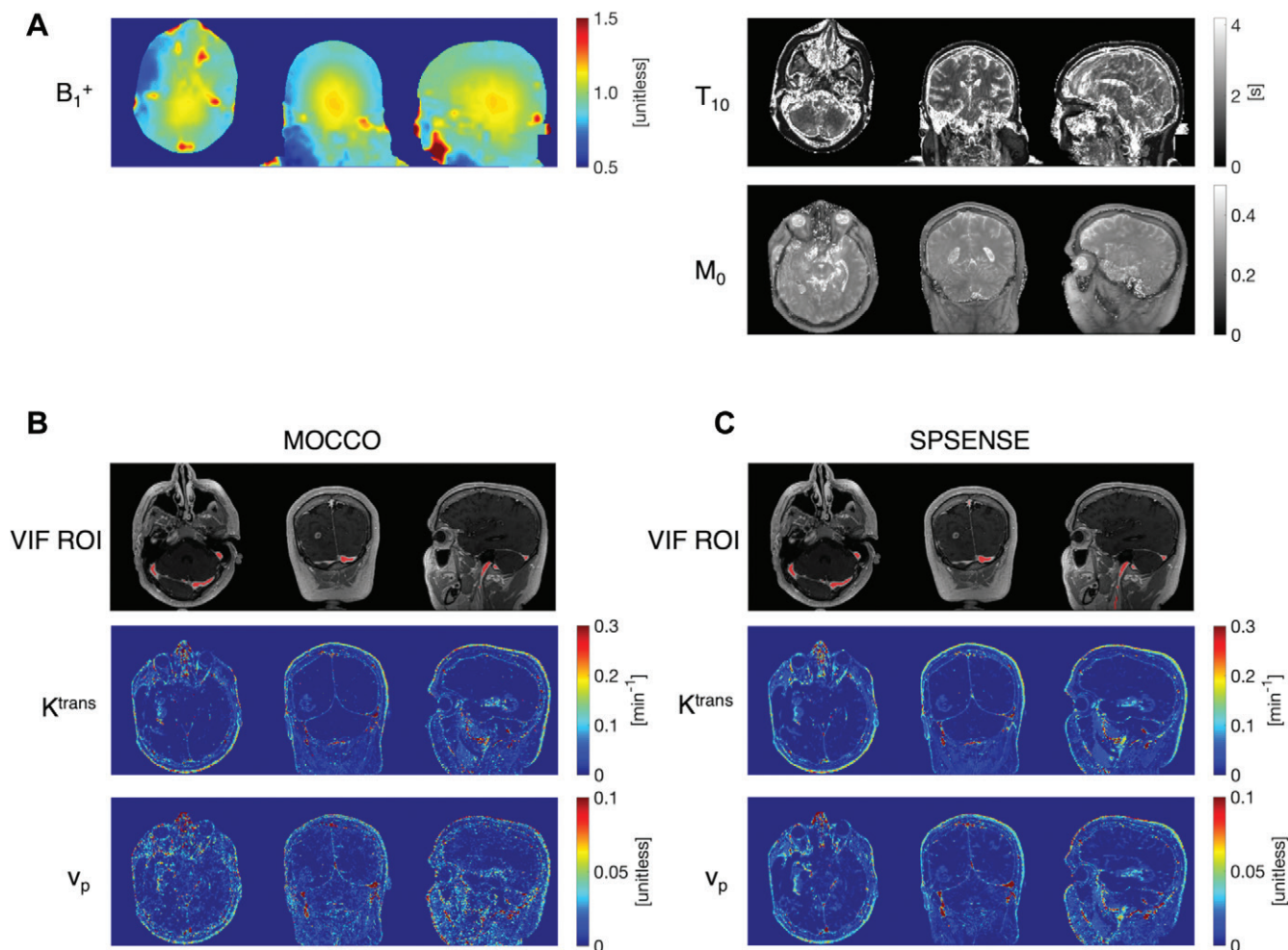


**Figure 3:** Representative parameter maps of dynamic contrast-enhanced MRI examination in a 59-year-old woman in axial, coronal, and sagittal views for model consistency constrained (MOCCO) and sparse sensitivity encoding (SPSENSE) frameworks. A, Baseline maps for radiofrequency inhomogeneity ( $B_1^+$ ), baseline T1, and proton density map  $M_0$ . B, C, Images obtained after administration of contrast agent with regions of interest for vascular input functions on internal jugular veins, transverse and sigmoid dural venous sinuses (red), plasma volume fraction ( $v_p$ ), and volume transfer constant ( $K^{trans}$ ) for MOCCO and SPSENSE, respectively.

(ie, time to peak, full width at 80% maximum, vesselness [tubularity of the spatial structure], and enhancement relative to period before administration of contrast agent) (this step was performed by Y.B., an MR scientist with 4 years of experience in brain DCE MRI) (18–21). We chose the largest connected vessel as a VIF region of interest (ROI). We then trimmed the outermost voxels to remove possible partial volume-averaging effects. The final VIF was jointly estimated (by Y.B.) from the magnitude of image voxels within the VIF ROI (22). Baseline proton density and T1 maps were estimated at matching spatial resolution and coverage from sparsely sampled  $B_1$ -corrected variable flip-angle T1 mapping (this step was performed by R.M.L., an MR scientist with 10 years of experience in brain DCE MRI) (17). For conversion of image intensity to concentration-time curves, we assumed the fast exchange limit approximation with fixed relaxivity ( $r_1 = 4.5 \text{ mM}^{-1} \text{ s}^{-1}$ ) and hematocrit value (45%). Concentration-time curves are assumed to follow the Patlak or extended Tofts-Kety model (23,24), where the appropriate tracer kinetic model was chosen on the basis of the Akaike information criterion (this step was performed by Y.B.) (25,26). To

account for bolus transit delay, we fit each voxel with three VIFs: one as extracted and two other functions shifted by plus and minus one time bin. For each voxel, the parameters of the best fit were retained.

The source code for data reconstruction and analysis can be found on GitHub ([https://github.com/usc-mrell/dcemri\\_pseudo\\_test\\_retest](https://github.com/usc-mrell/dcemri_pseudo_test_retest); revision b2b3e4b).

### Statistical Analysis

To determine reproducibility of VIF estimation, we determined the within-case coefficient of variation (COV) (27,28) and reproducibility coefficient (RC) (27) of relevant VIF features (this step was performed by Y.B.) (28–30). Specifically, we determined (a) peak concentration and (b) area under the curve, both of which are crucial for accurate tracer-kinetic estimation, and (c) area under the first pass, which is important for cerebral blood flow measurement.

The advent of high-spatial-resolution DCE MRI protocols has led to increased interest in histogram analyses and histogram-derived statistics to analyze tumor heterogeneity (31). To determine reproducibility of histogram analysis of



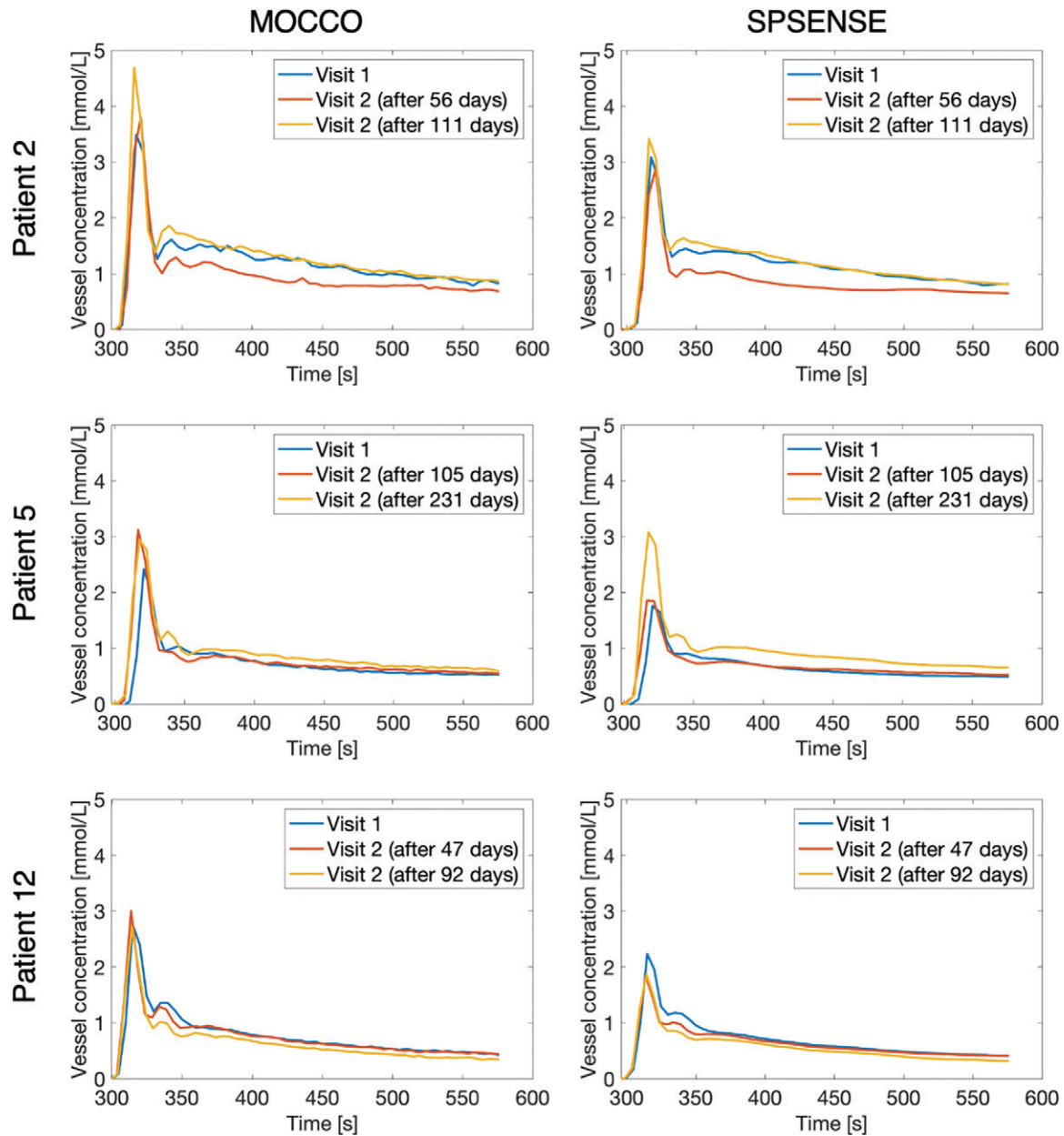


**Figure 4:** Graphs show representative vascular input functions (VIFs) for different participants, visits, and methods. Each row corresponds to a different participant. Left column shows model consistency constrained (MOCCO) reconstruction, and right column shows VIFs estimated from sparse sensitivity encoded (SPSENSE) image time series. All VIFs show blood concentration.

tracer kinetic parameters, ROIs were manually drawn on five different enhancing tissue types: normal-appearing white matter, the mucosal surface of the nasal mucosa, the choroid plexus, scalp fat, and the temporalis muscle (performed by Y.B. and J.A., a board-certified neuroradiologist with 9 years of experience in head, neck, and spine imaging). The ROIs were not drawn on tumor tissue because of postresection ambiguity and possible tumor progression.

To determine reproducibility of potential markers and the underlying histograms for tracer-kinetic parameters—plasma volume fraction ( $v_p$ ) and volume transfer constant ( $K^{trans}$ )—we computed the COV and RC for the robust histogram statistics of median and 95th percentile (this step

was performed by Y.B.) (13,15). Statistical analysis was performed in Matlab, version R2018a (MathWorks).

## Results

### Participant Characteristics

We estimated reproducibility of the proposed pipeline using the DCE MRI examinations of 13 participants with high-grade glioma (mean age  $\pm$  standard deviation, 61 years  $\pm$  10; nine women). Table E1 (online) summarizes participant demographic characteristics, tumor types, and time intervals between successive examinations. A flowchart illustrating recruitment of 32 patients with brain tumors and the

**Table 1: Mean Values, Within-Patient Coefficient of Variation, and Reproducibility Coefficient for Features Derived from Vascular Input Functions**

Variable	MOCCO			SPSENSE		
	Mean	COV	RC	Mean	COV	RC
Peak concentration	3.08	0.22	1.67	2.09	0.15	0.84
Area under curve	247.49	0.18	124.63	209.58	0.13	83.19
Area under first pass	46.02	0.21	24.0	35.05	0.16	16.57

Note.—Peak concentration is presented in millimoles per liter. Area under curve and area under first pass are presented in millimoles at 1 second per liter. Reproducibility was determined for model consistency constrained (MOCCO) and sparse sensitivity encoded (SPSENSE) vascular input function estimation. All values refer to blood concentration. COV = coefficient of variation, RC = reproducibility coefficient.

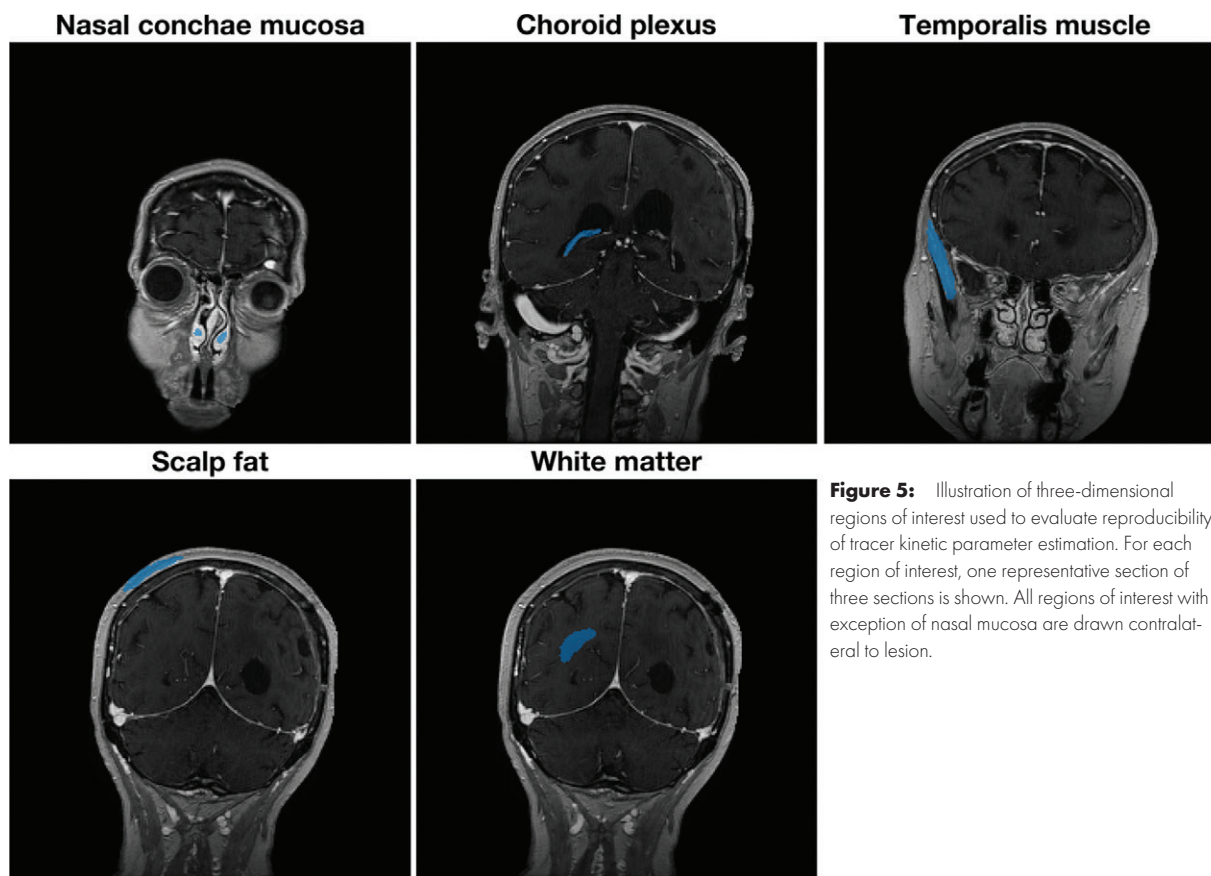


**Figure 5:** Illustration of three-dimensional regions of interest used to evaluate reproducibility of tracer kinetic parameter estimation. For each region of interest, one representative section of three sections is shown. All regions of interest with exception of nasal mucosa are drawn contralateral to lesion.

criteria for exclusion of 19 participants from this study is shown in Figure 1.

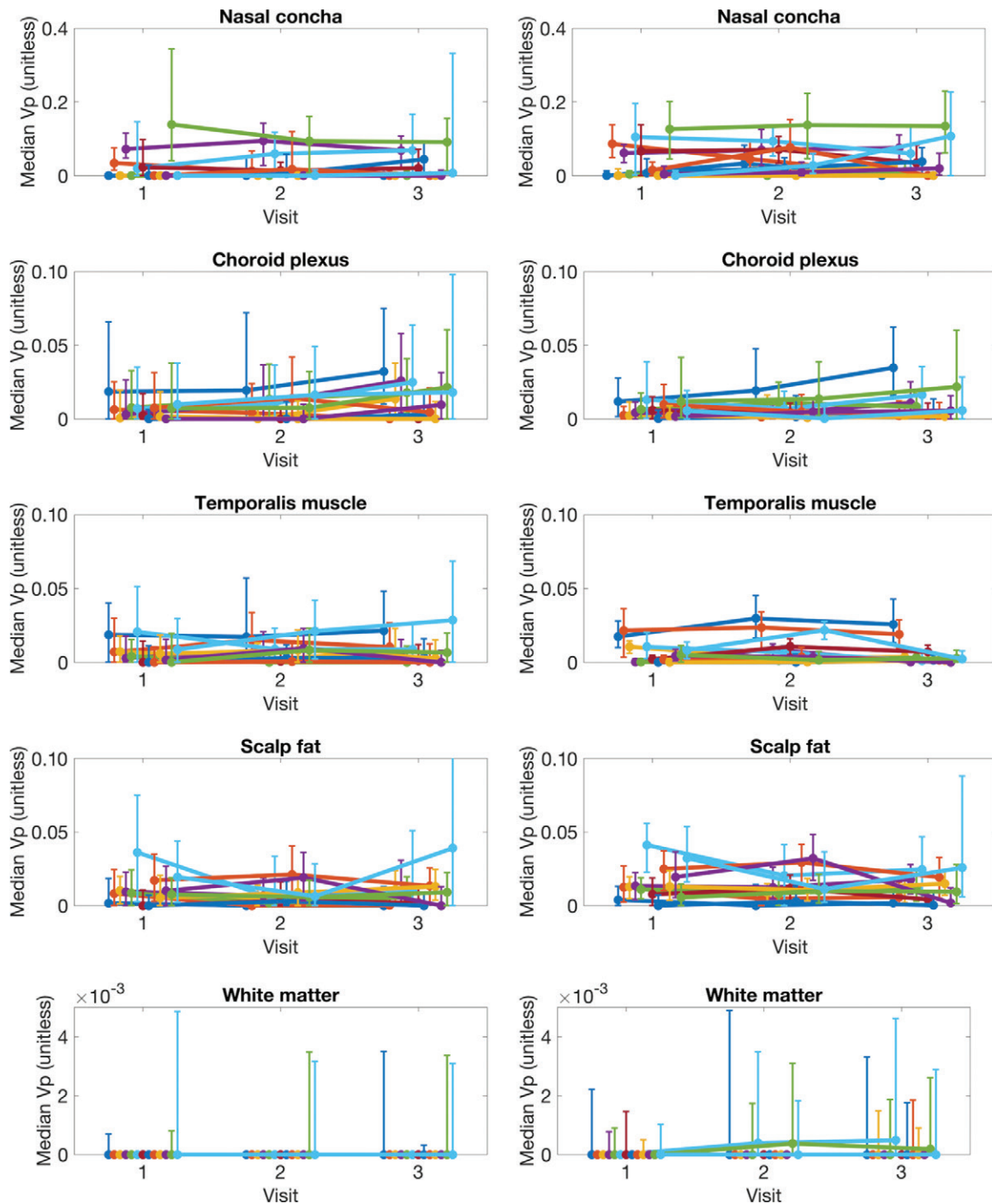
### DCE MRI Examination

Figure 3 illustrates outputs of the fully automated DCE MRI pipeline for one representative tumor case in a 59-year-old woman. It includes spatial maps of  $B_1^+$ , precontrast-agent T1, and proton density  $M_0$  maps; VIF ROI location; and tracer-kinetic parameters. The  $B_1^+$ , T1, and  $M_0$  maps are common to both methods. MOCCO and SPSENSE estimation approaches differ in VIF estimation and in estimated parameter maps for  $v_p$  and  $K^{\text{trans}}$ . Using both approaches, the internal jugular veins, transverse, and sigmoid dural venous sinuses were detected.

**Table 2: Mean Volumes of Regions of Interest and Respective Number of Voxels for Tissue Types Shown in Figure 5**

Tissue Type	ROI Volume (mm <sup>3</sup> )	No. of Voxels
Nasal mucosa	370.7 ± 173.7	198 ± 93
Choroid plexus	982.6 ± 399.6	524 ± 213
Temporalis muscle	2096.0 ± 1041.2	1118 ± 555
Scalp fat	1145.2 ± 313.2	611 ± 167
White matter	1321.5 ± 268.1	705 ± 143

Note.—Data are presented as means ± standard deviation. ROI = region of interest.



**Figure 6:** Graphs show temporal evolution of median plasma volume fraction ( $v_p$ ) in five regions of interest shown in Figure 5 for different lesions and visits. Each row corresponds to different tissue. Left column shows results for model consistency constrained reconstruction, and right column shows sparse sensitivity encoded reconstruction. Each line corresponds to different participant. Error bars show interquartile range (25th to 75th percentile) for each participant, visit, and tissue region of interest.

### Reproducibility of Patient-specific VIF Estimation

Figure 4 shows representative VIFs for three participants at three visits each. The VIFs are measured with MOCCO and derived from SPSENSE image time series data. Table 1 lists mean, COV, and reproducibility coefficients for peak concentration, areas under the curve, and areas under the first pass. VIFs estimated in the MOCCO framework were larger in

magnitude than SPSENSE-based VIF estimation, with mean area under the curve of 247.5 mM for MOCCO versus 209.6 mM for SPSENSE. The COVs for VIF features were 0.18 for MOCCO and 0.13 for SPSENSE, indicating similar reproducibility of MOCCO and SPSENSE in their ability to measure VIFs. As shown in Figure 4 and Table 1, estimation of VIFs based on the MOCCO method led to overall larger initial enhance-

**Table 3: Reproducibility of Histogram Statistics for Plasma Volume Fraction**

Variable	MOCCO			SPSENSE		
	Mean	COV	RC	Mean	COV	RC
$v_p$ median*						
Nasal mucosa	0.02	0.87	0.04	0.04	0.92	0.07
Choroid plexus	0.01	1.17	0.02	0.01	0.53	0.01
Temporalis muscle	0.01	0.94	0.01	0.01	0.95	0.01
Scalp fat	0.01	1.00	0.02	0.01	0.65	0.02
White matter	0.00	...	0.00	0.00	...	0.00
$v_p$ 95th percentile†						
Nasal mucosa	0.20	0.77	0.60	0.20	0.57	0.50
Choroid plexus	0.09	0.35	0.10	0.05	0.33	0.05
Temporalis muscle	0.05	0.21	0.04	0.03	0.37	0.03
Scalp fat	0.07	0.34	0.11	0.05	0.27	0.05
White matter	0.01	0.88	0.01	0.01	0.39	0.01

Note.—Reproducibility was determined for model consistency constrained (MOCCO) and sparse sensitivity encoded (SPSENSE) vascular input function estimation. All values are unitless. COV = coefficient of variation, RC = reproducibility coefficient,  $v_p$  = plasma volume fraction.

\* Mean, COV, and RC for the median of  $v_p$  histograms in the five different regions of interest shown in Figure 5.

† Mean, COV, and RC for the 95th percentile of  $v_p$  histograms.

ment peaks of the VIF, with mean peak concentration of 3.1 mM compared with 2.1 mM for SPSENSE.

### ROI Placement

Figure 5 illustrates all five three-dimensional ROIs used to compute histogram statistics and to assess their reproducibility. With the exception of the nasal mucosa, all ROIs are drawn contralateral to the lesion. All ROIs spanned at least three sagittal sections. To illustrate the number of data points composing the individual histograms for each ROI, the mean and standard deviation of the ROI sizes for each tissue type are listed in Table 2.

### Reproducibility of $v_p$ Estimation

Figure 6 shows the temporal evolution of median for  $v_p$  per region as estimated by MOCCO and SPSENSE. Table 3 lists the mean, COV, and RC for the histogram statistics median and 95th percentile for  $v_p$ . As illustrated in Figure 6, both methods led to similar temporal behavior for median  $v_p$  across the three visits for the three largest ROIs (ie, temporalis muscle, scalp fat, and white matter). Inpatient variation across time was similar to interpatient variation across different participants. MOCCO achieved COVs of 87%–117% for median  $v_p$  in healthy tissue, whereas SPSENSE achieved COVs of 53%–95% for median  $v_p$ . RCs for the median  $v_p$  are below 0.04 and 0.07 for MOCCO and SPSENSE, respectively. This maximum was achieved in the most strongly vascularized nasal mucosa.

### Reproducibility of $K^{trans}$ Estimation

Figure 7 shows the temporal evolution of median for  $K^{trans}$  per region as estimated by MOCCO and SPSENSE. Table 4 lists the mean, COV, and RC for the histogram statistics of median and 95th percentile for  $K^{trans}$ . In nasal mucosa, temporalis muscle, and scalp fat, the median  $K^{trans}$  values estimated by the SPSENSE method (0.46 min<sup>-1</sup>, 0.05 min<sup>-1</sup>, and 0.05 min<sup>-1</sup>, respectively)

were on average higher than those estimated by MOCCO (0.41 min<sup>-1</sup>, 0.04 min<sup>-1</sup>, and 0.38 min<sup>-1</sup>, respectively), which is in alignment with lower peak VIF amplitude of SPSENSE. MOCCO achieved COVs of 31%–91% for median  $K^{trans}$  in healthy tissue. SPSENSE achieved COVs of 29%–57% for median  $K^{trans}$ . For the two largest tissue ROIs with nonnegligible  $K^{trans}$  (ie, temporalis muscle and scalp fat), both methods estimated median  $K^{trans}$  with COVs of 31%–50%, and the higher valued 95th percentile with COVs of 22%–32%. For thinner structures, such as the choroid plexus, or measurements of high permeability, such as the 95th percentile of  $K^{trans}$  in the nasal mucosa, the COV was as high as 60%–91%. Similarly, RC estimates increased with increased parameter magnitude or tenuity of the underlying tissue structure. With use of the SPSENSE method, the protocol estimated median  $K^{trans}$  in healthy tissues with a maximum RC of 0.06 min<sup>-1</sup> in large, low-enhancing tissue regions, such as muscle and fat. The maximum reproducibility coefficient for the median  $K^{trans}$  was, however, as high as 0.48 min<sup>-1</sup> in smaller or more strongly enhancing tissue regions, such as the choroid plexus or nasal mucosa.

Results of reproducibility for estimation of the extravascular-extracellular volume fraction are shown in Figure E1 and Table E2 (both online).

### Discussion

Advances in sub-Nyquist-sampled dynamic contrast-enhanced (DCE) MRI enables monitoring of brain tumors with millimeter spatial resolution and whole-brain coverage at 5-second temporal resolution. These new features require evaluation regarding achievable test-retest reproducibility in DCE MRI measurements. We estimate that millimeter-resolution whole-brain DCE MRI can be used to estimate the median volume transfer constant in healthy tissues with maximum reproducibility coefficient (RC) of 0.06 min<sup>-1</sup> in large, low-enhancing tissue regions,



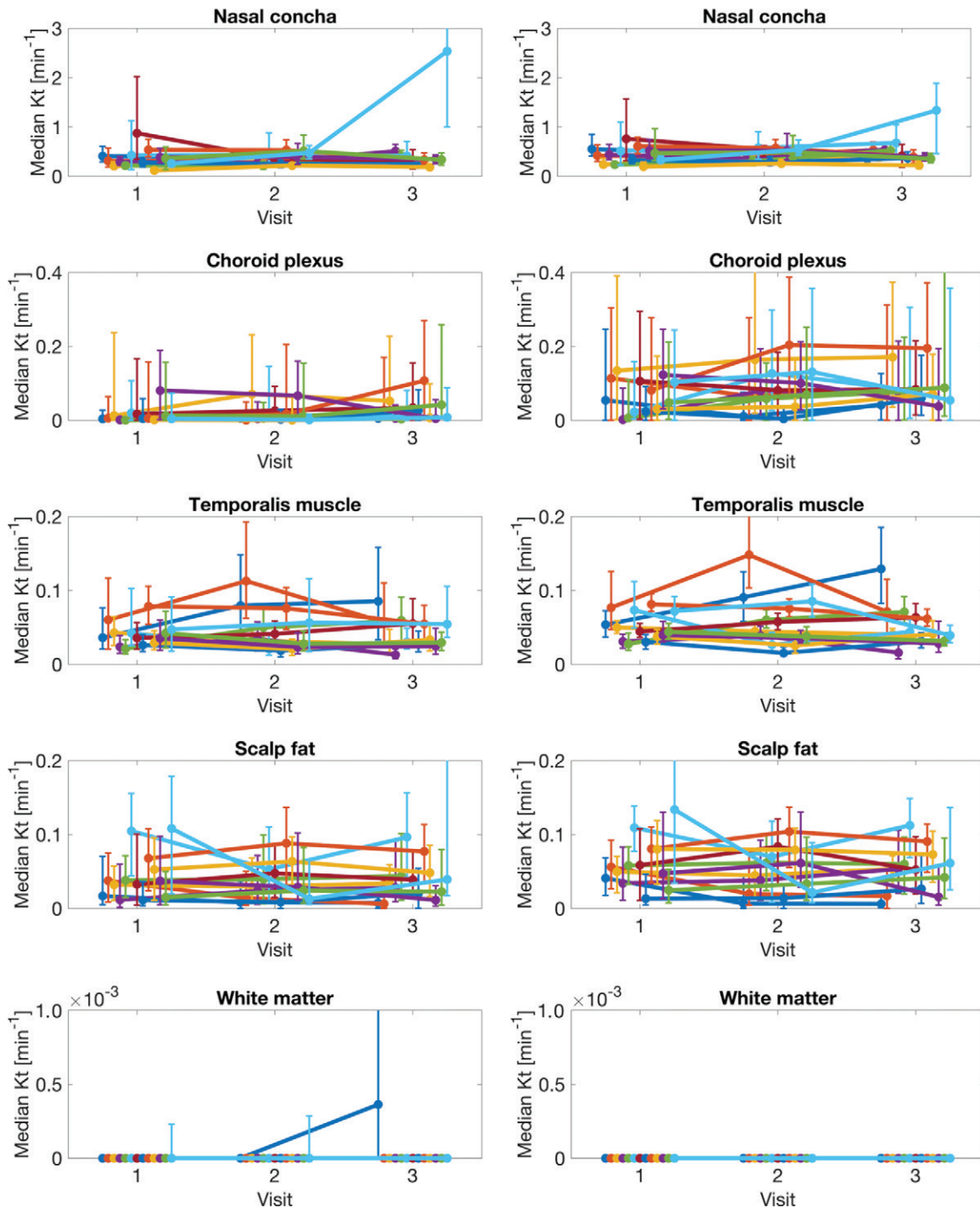


**Figure 7:** Graphs show evolution of median volume transfer constant ( $K^{\text{trans}}$ ) in five regions of interest shown in Figure 5 for different lesions and visits. Each row corresponds to different tissue. Left column shows results for model consistency constrained reconstruction, and right column shows results for sparse sensitivity encoded reconstruction. Each line corresponds to different participant. Error bars show interquartile range (25th to 75th percentile) for each participant, visit, and tissue region of interest.

such as muscle and fat, and maximum RC less than  $0.48 \text{ min}^{-1}$  in smaller or more strongly enhancing tissue regions, such as the choroid plexus or nasal mucosa.

We estimate that millimeter-resolution whole-brain DCE MRI can achieve a maximum COV in healthy tissues less than 57% and 91% for median  $K^{\text{trans}}$  with use of SPSENSE and MOCCO, respectively. In larger, potentially more homogeneous structures (eg, the temporalis muscle or scalp fat),

the COV for median  $K^{\text{trans}}$  is estimated to be 30%–50% for both methods. As a reference, the current Radiological Society of North America Quantitative Imaging Biomarkers Alliance DCE profile specifies an achievable COV of 20% for mean  $K^{\text{trans}}$  in a tumor ROI of at least 2 cm in diameter, which requires a longitudinal change of 40% in  $K^{\text{trans}}$  for statistical significance (13). If confirmed in larger cohorts, then the COVs found in this study would imply that even the best method may

**Table 4: Reproducibility of Histogram Statistics for Volume Transfer Constant**

Variable	MOCCO			SPSENSE		
	Mean (min <sup>-1</sup> )	COV	RC (min <sup>-1</sup> )	Mean (min <sup>-1</sup> )	COV	RC (min <sup>-1</sup> )
<b>K<sup>trans</sup> median*</b>						
Nasal mucosa	0.41	0.42	1.02	0.46	0.29	0.48
Choroid plexus	0.02	0.91	0.06	0.08	0.57	0.10
Temporalis muscle	0.04	0.31	0.04	0.05	0.33	0.06
Scalp fat	0.04	0.46	0.05	0.05	0.49	0.06
White matter	0.00	...	0.00	0.00	...	0.00
<b>K<sup>trans</sup> 95th percentile†</b>						
Nasal mucosa	1.74	0.66	8.18	1.67	0.61	5.19
Choroid plexus	0.34	0.38	0.36	0.55	0.23	0.36
Temporalis muscle	0.16	0.27	0.13	0.13	0.32	0.14
Scalp fat	0.19	0.26	0.22	0.16	0.22	0.12
White matter	0.00	...	0.01	0.00	...	0.00

Note.—Reproducibility was determined for model consistency constrained (MOCCO) and sparse sensitivity encoded (SPSENSE) vascular input function estimation. COV = coefficient of variation, K<sup>trans</sup> = volume transfer constant, RC = reproducibility coefficient.

\* Mean, COV, and RC for the median of K<sup>trans</sup> histograms in the five different regions of interest shown in Figure 5.

† Mean, COV, and RC for the 95th percentile of K<sup>trans</sup> histograms.

not yield parameters sensitive enough to monitor subtle longitudinal changes in brain tumors. Differences in estimated COV may be attributed to differences in the use of tracer-kinetic models (which is specified as the standard Tofts model in the profile), estimation of COV in tissues with possibly different permeability strengths (ie, tumor tissue vs healthy tissues) or the time gaps between repeated measurements.

High-spatial-resolution whole-brain DCE MRI guarantees the existence of large-vessel structures inside the field of view. Minimal inflow enhancement and partial volume corruption in the vessel region greatly facilitate automation of VIF estimation. Automation has been a major bottleneck in the standardization of DCE MRI, and the proposed approach helps facilitate automation. We expect that such automation can expedite translation, similar to how fully automated software packages for stroke MRI analysis provide a powerful way to standardize postprocessing and pave the road to clinical deployment (32).

Bias and linearity of DCE MRI cannot be assessed in vivo because of lack of ground-truth values. Therefore, DCE MRI is predominantly suited for longitudinal monitoring, where bias cancels but assessment requires a high degree of known precision (15). We analyzed and characterized reproducibility of the automated DCE MRI method in several different tissues with different enhancement characteristics. Knowledge of the RC of a given method is a crucial first step in determining the detectable effect size in longitudinal studies, such as response to therapy assessment (15).

Our study had several limitations. First, there was a lack of tracer-kinetic parameter ground truth for validation. This limitation is common to most evaluations of DCE MRI pipelines. Estimation of the VIF is a crucial intermediate step and could be cross validated with CT measurements in phantoms (33). For breast DCE MRI, a partial alternative would be to deploy the Stewart-Hamilton theorem to validate the area under the initial peak through independent cardiac output measurements (28). Second,

this study used reference regions, not brain tumor tissue. Test-retest studies in sick patients (eg, those with high-grade glioma) and involving procedures with contrast agents are notoriously difficult to conduct because they require patients to appear for additional non-standard-of-care MRI examinations. They are rarely performed despite being an integral part on the path to clinical deployment. Typically, clinical studies are cascaded from pilot studies to randomized clinical trials. For this reason, we pursued a pseudo test-retest study design by selecting tissues that were deemed to be stable during regular treatment follow-up examinations. This relies on the assumption of no or negligible change in the chosen tissues between the time points, which erroneously increases estimated measures of reproducibility if violated. However, because of lack of ground truth and standard reference methods, this assumption may be hard to verify rigorously through nonradiographic measures. As a result of the severity and aggressiveness of the disease, these tissue types do not include the actual tumor target tissue, where possibility of tumor growth and change could not be eliminated. Future research is needed to show whether few representative (healthy) tissue types at various enhancement strength can accurately represent and capture the potential diverse characteristics of reproducibility in lesions as heterogeneous as brain tumors. Finally, our study relied on several simplifying model assumptions. These assumptions include a constant relaxivity and hematocrit value. Hematocrit is known to change throughout the course of treatment (28). We did not model water exchange (34), diffusion of contrast agent (35), or damage to tissue after surgery, which can lead to additional leakage.

We demonstrate a fully automated dynamic contrast-enhanced (DCE) MRI reconstruction and modeling pipeline offering high spatial and temporal resolution with full brain coverage. This includes fast T1 estimation before administration of contrast agents, automated vascular input function extraction, and model-based tracer kinetic parameter mapping. We further demonstrate pseudo test-retest as a possible alternative to assess

reproducibility in sick patients. On the basis of the large parameter range for volume transfer constant covered by the various tissue types in this study, we believe that reproducibility in these tissues can give guidance to future study designs involving high-spatiotemporal-resolution DCE MRI.

**Acknowledgment:** We thank Samuel R. Barnes, PhD, for providing Gpufit, fast GPU-accelerated fitting to tracer-kinetic models (24).

**Author contributions:** Guarantors of integrity of entire study, Y.B., K.S.N.; study concepts/study design or data acquisition or data analysis/interpretation, all authors; manuscript drafting or manuscript revision for important intellectual content, all authors; approval of final version of submitted manuscript, all authors; agrees to ensure any questions related to the work are appropriately resolved, all authors; literature research, Y.B., R.M.L., K.S.N.; clinical studies, R.M.L., R.F.; experimental studies, Y.B., R.M.L., R.F.; statistical analysis, Y.B., J.A.; and manuscript editing, all authors

**Disclosures of Conflicts of Interest:** Y.B. disclosed no relevant relationships. R.M.L. Activities related to the present article: disclosed no relevant relationships. Activities not related to the present article: is employed by GE Healthcare; holds stock/stock options in GE. Other relationships: disclosed no relevant relationships. J.A. Activities related to the present article: disclosed no relevant relationships. Activities not related to the present article: is a consultant for Medtronic. Other relationships: disclosed no relevant relationships. R.F. disclosed no relevant relationships. K.S.N. Activities related to the present article: disclosed no relevant relationships. Activities not related to the present article: has grants/grants pending with Siemens Healthineers; received payment for travel/accommodations/meeting expenses unrelated to activities listed from Siemens Healthineers; receives research support from GE Healthcare and Siemens Healthineers. Other relationships: has a pending patent filed by USC.

## References

- Bonekamp D, Deike K, Wiestler B, et al. Association of overall survival in patients with newly diagnosed glioblastoma with contrast-enhanced perfusion MRI: Comparison of intraindividually matched T1 - and T2 (\*) -based bolus techniques. *J Magn Reson Imaging* 2015;42(1):87–96.
- Kickingreder P, Wiestler B, Graf M, et al. Evaluation of dynamic contrast-enhanced MRI derived microvascular permeability in recurrent glioblastoma treated with bevacizumab. *J Neurooncol* 2015;121(2):373–380.
- Cao Y. The promise of dynamic contrast-enhanced imaging in radiation therapy. *Semin Radiat Oncol* 2011;21(2):147–156.
- Guo Y, Lebel RMM, Zhu Y, et al. High-resolution whole-brain DCE-MRI using constrained reconstruction: Prospective clinical evaluation in brain tumor patients. *Med Phys* 2016;43(5):2013–2023.
- Kurland BF, Gerstner ER, Mountz JM, et al. Promise and pitfalls of quantitative imaging in oncology clinical trials. *Magn Reson Imaging* 2012;30(9):1301–1312.
- Cuenod CA, Balvay D. Perfusion and vascular permeability: basic concepts and measurement in DCE-CT and DCE-MRI. *Diagn Interv Imaging* 2013;94(12):1187–1204.
- Guo Y, Lingala SG, Zhu Y, Lebel RM, Nayak KS. Direct estimation of tracer-kinetic parameter maps from highly undersampled brain dynamic contrast enhanced MRI. *Magn Reson Med* 2017;78(4):1566–1578.
- Dikaos N, Arridge S, Hamy V, Punwani S, Atkinson D. Direct parametric reconstruction from undersampled (k, t)-space data in dynamic contrast enhanced MRI. *Med Image Anal* 2014;18(7):989–1001.
- Feng L, Grimm R, Block KT, et al. Golden-angle radial sparse parallel MRI: combination of compressed sensing, parallel imaging, and golden-angle radial sampling for fast and flexible dynamic volumetric MRI. *Magn Reson Med* 2014;72(3):707–717.
- Lebel RM, Jones J, Ferre JC, Law M, Nayak KS. Highly accelerated dynamic contrast enhanced imaging. *Magn Reson Med* 2014;71(2):635–644.
- Lingala SG, Guo Y, Bliesener Y, et al. Tracer kinetic models as temporal constraints during brain tumor DCE-MRI reconstruction. *Med Phys* 2020;47(1):37–51.
- Guo Y, Lingala SG, Bliesener Y, Lebel RM, Zhu Y, Nayak KS. Joint arterial input function and tracer kinetic parameter estimation from undersampled dynamic contrast-enhanced MRI using a model consistency constraint. *Magn Reson Med* 2018;79(5):2804–2815.
- RSNA QIBA Profiles. <http://qibawiki.rsna.org/index.php/Profiles>. Accessed November 5, 2019.
- Hutterer M, Hattingen E, Palm C, Proescholdt MA, Hau P. Current standards and new concepts in MRI and PET response assessment of antiangiogenic therapies in high-grade glioma patients. *Neuro Oncol* 2015;17(6):784–800.
- Shukla-Dave A, Obuchowski NA, Chenevert TL, et al. Quantitative imaging biomarkers alliance (QIBA) recommendations for improved precision of DWI and DCE-MRI derived biomarkers in multicenter oncology trials. *J Magn Reson Imaging* 2019;49(7):e101–e121.
- Sacolick LI, Wiesinger F, Hancu I, Vogel MW. B1 mapping by Bloch-Siegert shift. *Magn Reson Med* 2010;63(5):1315–1322.
- Lebel RM, Guo Y, Zhu Y, et al. The comprehensive contrast-enhanced neuro exam [abstr]. In: Proceedings of the Twenty-Third Meeting of the International Society for Magnetic Resonance in Medicine. Berkeley, Calif: International Society for Magnetic Resonance in Medicine, 2015; 4456.
- Shanbhag DD, Gupta SN, Rajamani KT, Zhu Y, Mullick R. A generalized methodology for detection of vascular input function with dynamic contrast enhanced perfusion data [abstr]. In: Proceedings of the Twentieth Meeting of the International Society for Magnetic Resonance in Medicine. Berkeley, Calif: International Society for Magnetic Resonance in Medicine, 3524.
- Jacobs M, Benovoy M, Chang LC, Arai AE, Hsu LY. Evaluation of an automated method for arterial input function detection for first-pass myocardial perfusion cardiovascular magnetic resonance. *J Cardiovasc Magn Reson* 2016;18(1):17.
- Chan SLS, Gal Y. Automatic detection of arterial voxels in dynamic contrast-enhanced MR images of the brain. In: 2012 International Conference on Digital Image Computing Techniques and Applications (DICTA), Fremantle, Australia, December 3–5, 2012. Piscataway, NJ: IEEE, 2012; 1–7.
- Frangi AF, Niessen WJ, Vincken KL, Viergever MA. Multiscale vessel enhancement filtering. In: Wells WM, Colchester A, Delp S, eds. Medical Image Computing and Computer-Assisted Intervention — MICCAI'98. MICCAI 1998. Lecture Notes in Computer Science, vol 1496. Cham, Switzerland: Springer, 1998; 130–137. <https://doi.org/10.1007/BFb0056195>.
- Klawer EME, van Houdt PJ, Simonis FFF, et al. Improved repeatability of dynamic contrast-enhanced MRI using the complex MRI signal to derive arterial input functions: a test-retest study in prostate cancer patients. *Magn Reson Med* 2019;81(5):3358–3369.
- Sourbron SP, Buckley DL. Classic models for dynamic contrast-enhanced MRI. *NMR Biomed* 2013;26(8):1004–1027.
- Barnes SR. Gpufit. <https://github.com/ironictoo/Gpufit>. Accessed October 16, 2019.
- Ewing JR, Bagher-Ebadian H. Model selection in measures of vascular parameters using dynamic contrast-enhanced MRI: experimental and clinical applications. *NMR Biomed* 2013;26(8):1028–1041.
- Lieberman G, Louzoun Y, Artzi M, Nadav G, Ewing JR, Ben Bashat D. DUSTER: dynamic contrast enhance up-sampled temporal resolution analysis method. *Magn Reson Imaging* 2016;34(4):442–450.
- Obuchowski NA, Reeves AP, Huang EP, et al. Quantitative imaging biomarkers: a review of statistical methods for computer algorithm comparisons. *Stat Methods Med Res* 2015;24(1):68–106.
- Georgiou L, Wilson DJ, Sharma N, Perren TJ, Buckley DL. A functional form for a representative individual arterial input function measured from a population using high temporal resolution DCE MRI. *Magn Reson Med* 2019;81(3):1955–1963.
- Li X, Cai Y, Moloney B, et al. Relative sensitivities of DCE-MRI pharmacokinetic parameters to arterial input function (AIF) scaling. *J Magn Reson* 2016;269:104–112.
- Lavini C. Simulating the effect of input errors on the accuracy of Tofts' pharmacokinetic model parameters. *Magn Reson Imaging* 2015;33(2):222–235.
- Just N. Improving tumour heterogeneity MRI assessment with histograms. *Br J Cancer* 2014;111(12):2205–2213.
- Bang OY, Chung JW, Son JP, et al. Multimodal MRI-based triage for acute stroke therapy: Challenges and progress. *Front Neurol* 2018;9:586.
- Foltz W, Driscoll B, Laurence Lee S, et al. Phantom validation of DCE-MRI magnitude and phase-based vascular input function measurements. *Tomography* 2019;5(1):77–89.
- Li X, Rooney WD, Springer CS Jr. A unified magnetic resonance imaging pharmacokinetic theory: intravascular and extracellular contrast reagents. *Magn Reson Med* 2005;54(6):1351–1359.
- Fluckiger JU, Loveless ME, Barnes SL, Lepage M, Yankeelov TE. A diffusion-compensated model for the analysis of DCE-MRI data: theory, simulations and experimental results. *Phys Med Biol* 2013;58(6):1983–1998.